arXiv:1604.02124v3 [cond-mat.mtrl-sci] 12 Apr 2016

Magnetic and noncentrosymmetric Weyl fermion semimetals in the RAlX family of compounds (R=rare earth, Al=aluminium, X=Si, Ge)

Guoqing Chang*,[1,2] Bahadur Singh*,[1,2] Su-Yang Xu*†,[3] Guang Bian,[3] Shin-Ming Huang,[1,2,4] Chuang-Han Hsu,[1,2] Ilya Belopolski,[3] Nasser Alidoust,[3] Daniel S. Sanchez,[3] Hao Zheng,[3] Hong Lu,[5] Xiao Zhang,[5] Yi Bian,[5] Tay-Rong Chang,[6] Horng-Tay Jeng,[6,7] Arun Bansil,[8] Han Hsu,[9] Shuang Jia,[5,10] Titus Neupert,[11] Hsin Lin†,[1,2] and M. Zahid Hasan†[3]

[1]*Centre for Advanced 2D Materials and Graphene Research Centre National University of Singapore, 6 Science Drive 2, Singapore 117546*

[2]*Department of Physics, National University of Singapore, 2 Science Drive 3, Singapore 117542*

[3]*Laboratory for Topological Quantum Matter and Spectroscopy (B7), Department of Physics, Princeton University, Princeton, New Jersey 08544, USA*

[4]*Department of Physics, National Sun Yat-Sen University, Kaohsiung 804, Taiwan*

[5]*International Center for Quantum Materials, School of Physics, Peking University, China*

[6]*Department of Physics, National Tsing Hua University, Hsinchu 30013, Taiwan*

[7]*Institute of Physics, Academia Sinica, Taipei 11529, Taiwan*

[8]*Department of Physics, Northeastern University, Boston, Massachusetts 02115, USA*

[9]*Department of Physics, National Central University, Jhongli City, Taoyuan 32001, Taiwan*

[10]*Collaborative Innovation Center of Quantum Matter, Beijing,100871, China*

[11]*Princeton Center for Theoretical Science, Princeton University, Princeton, New Jersey 08544, USA*

(Dated: April 13, 2016)

* These authors contributed equally to this work.

† Corresponding authors (emails): suyangxu@princeton.edu, nilnish@gmail.com, mzhasan@princeton.edu

Abstract

Weyl semimetals are novel topological conductors that host Weyl fermions as emergent quasiparticles. While the Weyl fermions in high-energy physics are strictly defined as the massless solution of the Dirac equation and uniquely fixed by Lorentz symmetry, there is no such constraint for a topological metal in general. Specifically, the Weyl quasiparticles can arise by breaking either the space-inversion ($\mathcal{I}$) or time-reversal ($\mathcal{T}$) symmetry. They can either respect Lorentz symmetry (type-I) or strongly violate it (type-II). To date, different types of Weyl fermions have been predicted to occur only in different classes of materials. In this paper, we present a significant materials breakthrough by identifying a large class of Weyl materials in the RAlX (R=Rare earth, Al, X=Ge, Si) family that can realize all different types of emergent Weyl fermions ($\mathcal{I}$-breaking, $\mathcal{T}$-breaking, type-I or type-II), depending on a suitable choice of the rare earth elements. Specifically, RAlX can be ferromagnetic, nonmagnetic or antiferromagnetic and the electronic band topology and topological nature of the Weyl fermions can be tuned. The unparalleled tunability and the large number of compounds make the RAlX family of compounds a unique Weyl semimetal class for exploring the wide-ranging topological phenomena associated with different types of emergent Weyl fermions in transport, spectroscopic and device-based experiments.

Finding new quantum materials with useful properties is one of the frontiers of modern condensed matter physics and material science [1–4]. Very recently, a new and fascinating topological metallic phase of matter, the Weyl semimetal [5–15], has attracted significant attention because of the physical phenomena enabled by its unique topological properties. In contrast to Weyl fermions in high-energy physics, which travel exactly at the speed of light and strictly obey Lorentz invariance, the emergent Weyl fermions in a Weyl semimetal are not subject to these restrictions. They can be classified into type-I Weyl fermions that respect Lorentz symmetry and have a typical conical dispersion and type-II Weyl fermions that dramatically violate Lorentz symmetry and manifest in a tilted-over cone in energy-momentum space [16]. This distinction is expected to critically affect both the negative magnetoresistance associated with Weyl fermions through the chiral anomaly in the bulk [17, 18] as well as the nonlocal transport caused by the Fermi arcs on the surface [19, 20]. On the other hand, emergent Weyl fermions can also be categorized by their symmetry-breaking origin. Fundamentally, they can only arise if the crystal breaks either time-reversal ($\mathcal{T}$) or space inversion ($\mathcal{I}$) symmetry. The $\mathcal{T}$-breaking and $\mathcal{I}$-breaking Weyl semimetals are expected to exhibit distinct topological responses in transport and spectroscopic experiments [21]. For example, a $\mathcal{T}$-breaking Weyl semimetal is expected to show an anomalous Hall response [22] in electrical transport and Faraday/Kerr rotations in optical experiments [23]. When confining a magnetic Weyl semimetal into 2D, e.g., into a monolayer, the anomalous Hall conductance and Faraday/Kerr rotations can become quantized [24], which means that the system becomes a quantum anomalous Hall insulator or a Chern insulator. On the other hand, an $\mathcal{I}$-breaking Weyl semimetal may exhibit a quantum spin (not charge) Hall effect in the monolayer limit [25]. In proximity to superconductivity, both $\mathcal{T}$-breaking and $\mathcal{I}$-breaking Weyl semimetals may become topological superconductors featuring Majorana fermions, but the induced superconductivity belongs to different topological classes [26–28].

In terms of material predictions, different types of emergent Weyl fermions have been proposed in very different material classes. The $\mathcal{I}$-breaking type-I Weyl fermions have been predicted [11, 12] and observed [13, 15] in TaAs and its close cousins, and the $\mathcal{T}$-breaking type-I Weyl fermions have been suggested in number of materials without experimental realization [9, 10, 24, 31, 32]. The $\mathcal{I}$-breaking type-II Weyl fermions have been predicted in the W(Mo)Te_2 class of materials [16, 29, 30], and the $\mathcal{T}$-breaking type-II Weyl fermions remain completely elusive. Very recently, we have experimentally discovered the first type-II

Weyl fermion semimetal in the rare-earth based compound, LaAlGe [33].

In this paper, we expand on this very recent experimental success [33] and theoretically identify a large class of Weyl semimetals in the RAlX (R=Rare earth, X=Ge, Si) family based on our systematic first-principles band structure calculations. We found that, depending on the choice of the rare earth elements, RAlX can be nonmagnetic (R=La), ferromagnetic (R=Ce, Pr) or antiferromagnetic (R=Sm, Gd). As a result, all different types of emergent Weyl fermions ($\mathcal{I}$-breaking and $\mathcal{T}$-breaking, type-I and type-II) can be realized in this class. The unparalleled tunability and the large number of compounds make the RAlX family a unique Weyl semimetal class for exploring the wide-ranging topological phenomena associated with different types of emergent Weyl fermions in transport and spectroscopic experiments.

Crystal structure and material considerations

RAlX crystallizes in a body-centered tetragonal Bravais lattice. The Ge-based compounds, RAlGe, are space-inversion breaking with a space group $I4_1md$ (109), point group C_{4v} [34–36] (Figs. 1**a,b**). The Si-based compounds, RAlSi, are space-inversion symmetric, with a space group $I4_1/amd$ (141), point group D_{4h} [37]. The recovery of inversion symmetry in RAlSi is likely due to the intermixing between Al and Si sites [37]. In the main text, we identify the Weyl semimetal states in the RAlGe compounds, and the RAlSi compounds will be briefly discussed in the supplementary information (SI).

We have grown single crystals of RAlX (R=La, Ce, Pr, Sm, Gd, X=Ge, Si) and studied their magnetic properties. Our results [38] are consistent with those reported in the existing literature [37, 39]. We mainly focus on the three compounds LaAlGe, CeAlGe, and PrAlGe. Our results [38] show that LaAlGe is nonmagnetic, whereas CeAlGe and PrAlGe are ferromagnetic with their Curie temperatures of 4.8 K and 17.0 K and their magnetization easy axes along the a and c directions, respectively. Figures 1**d-f** show the calculated density of states (DOS) without spin-orbit coupling (SOC) for LaAlGe, CeAlGe, and PrAlGe. The DOS of the majority and minority spin states are colored in red and blue. It can be seen clearly that in LaAlGe the DOS of the two spins are equal, consistent with its nonmagnetic nature. In contrast, an imbalance between the DOS of the majority and minority spin states is seen in CeAlGe and PrAlGe, suggesting a ferromagnetic ground state in agreement with the experimental finding [37–39]. The green shaded areas are the DOS of the f electrons.

The electronic configuration of La atom is [Xe]$6s^2 5d^1 4f^0$, meaning that all f orbitals are empty. Indeed, Fig. 1**d** shows that the all f electrons are in the conduction bands. On the other hand, a Ce (or Pr) atom should have 1 (or 2) electrons occupying the f orbitals. As a result, we see some f bands below the Fermi level ($E_{\rm F}$) in Figs. 1**e,f**. Moreover, our calculations (Figs. 1**e,f**) show that the occupied f electron states in CeAlGe and PrAlGe are clearly spin-polarized. These results suggest that the ferromagnetic coupling between the f electrons' local moments lead to ferromagnetism in CeAlGe and PrAlGe, which, in turn, makes the conduction electrons (s, p, d orbitals) near the Fermi level also spin-polarized.

In order to check this picture, we show the calculated band structure along high symmetry axes in Fig. 2. For the nonmagnetic LaAlGe, in absence of SOC (Fig. 2**a**), the majority spin and minority spin electron states are energetically degenerate. Further, it can be seen that the conduction and valence bands cross each other along the $\Gamma - \Sigma - N - \Sigma_1$ path, demonstrating a semimetal ground state. For the ferromagnetic CeAlGe and PrAlGe, our calculations (Figs. 2**b,c**) clearly show a spin splitting in the electronic states while the semimetallic nature is preserved. These results confirm our conceptual picture: The ferromagnetism arises from the ordering of the f electrons' local moments. These local moments serve as an effective Zeeman field and make the conduction (s, p, d orbital) bands spin polarized. Figures 2**d-f** show the band structure in the presence of SOC. Due to the lack of space-inversion symmetry, the bands of the nonmagnetic LaAlGe also become singly degenerate (spin polarized) upon including SOC. Because spin is not a good quantum number in the presence of SOC, we do not color code the bands in Figs. 2**d-f**. In general, the bands are singly degenerate in all three compounds with SOC.

Nonmagnetic space-inversion breaking Weyl semimetal state in LaAlGe

We now explore the existence of Weyl nodes in the nonmagnetic LaAlGe and their distribution in momentum space. For this, the crystal symmetries are key. Besides time-reversal $\mathcal{T}$ and translations, the symmetry group of LaAlGe contains a pair of mirror symmetries M_x, M_y that send $x \to -x$ and $y \to -y$, respectively, a four-fold screw-rotation $\bar{C}_4$ that is composed of a four-fold rotation symmetry C_4 around the z-axis and a translation by a $c/4$ in the z-direction, where c is the lattice constant in this direction, and a two-fold rotation C_2 around the z-axis, that is defined with respect to a different origin than $\bar{C}_4$. By combining $\bar{C}_4$ with M_x and M_y, we obtain a pair of glide mirror symmetries $\bar{M}_{xy}$ and $\bar{M}_{x\bar{y}}$.

In absence of SOC, the low-energy band structure contains the protected band degeneracies shown in Fig. 3**a**. The Σ point is encircled by a nodal line that arises as the conduction and valence bands cross each other on the mirror plane. As the bands have opposite mirror eigenvalue, they cannot hybridize on that plane, forming the nodal line. The $\bar{C}_4$ symmetry replicates this nodal line so that it appears four times in the BZ. This resembles the case of TaAs [11, 12]. In addition, we find four pairs of Weyl nodes near the $k_x = \pm k_y$ glide mirror planes. These Weyl nodes, that we will denote by W3, are pinned to $k_z = 0$ by the combined $C_2\mathcal{T}$ symmetry. (Notice that $C_2\mathcal{T}$ maps $k_z \to -k_z$.) Since they are arising without spin-orbit coupling, these nodes are doubly-degenerate (chiral charge ± 2), but linearly dispersing.

The inclusion of SOC lifts the degeneracy of the line nodes and the W3 nodes. In analogy with TaAs, from each line node there emerge three pairs of Weyl nodes that are arranged symmetrically about the mirror plane. One pair, denoted by W1, is pinned to $k_z = 0$ by the $C_2\mathcal{T}$ symmetry, the other two pairs, denoted W2, are mapped into each other under that symmetry and therefore appear at a nonzero k_z. Each W3 Weyl node is split into two Weyl nodes of the same unit chiral charge that we denote by W3' and W3". This splitting could in principle happen in two distinct ways that respect $C_2\mathcal{T}$: Either W3' and W3" share the same k_x, k_y, but appear at $+k_z$ and $-k_z$, or W3' and W3" have distinct k_x, k_y, and are pinned to $k_z = 0$. (See the Supplemental Information for a detailed discussion using an effective $k \cdot p$ model.) Our first-principle calculations evidence that the latter scenario is realized in LaAlGe. The distribution of the total of 40 Weyl nodes with SOC is shown in Fig. 3**b**. Figure 3**c** shows the top view of the Weyl node distribution. Only 32 nodes appear in this projection, as $C_2\mathcal{T}$-pairs of the W2 nodes of the same chirality are projected onto each other.

In addition, we discuss the energy positions and the other key properties of the Weyl nodes in LaAlGe. As shown in Fig. 3**i**, all W1 and W3 Weyl nodes are type-I and their energies are at least 60 meV above the Fermi level. On the other hand, the W2 Weyl nodes are type-II and they are located almost exactly at the Fermi level (see also Figs. 4**b,c**). Therefore, LaAlGe is a nonmagnetic, $\mathcal{I}$-breaking type-II Weyl semimetal. We have experientially demonstrated that in our recent photoemission study [33].

Ferromagnetic time-reversal breaking Weyl semimetal state in CeAlGe and

PrAlGe

We now turn to the Weyl semimetal states in CeAlGe and PrAlGe. We conceptually consider a temperature dependent evolution. Starting at a higher temperature above the Curie transition, we expect the Ce(Pr)AlGe sample to already become a Weyl semimetal because of the broken space-inversion symmetry. The Weyl semimetal state including the momentum space configuration of the Weyl nodes and other details should be very similar to those of LaAlGe. Now we lower the temperature below the Curie temperature so that the sample enters the ferromagnetic ground state. As we have elaborated before, the effect of the ferromagnetism in CeAlGe and PrAlGe can be understood qualitatively as a Zeeman coupling to the conduction electron states. To the lowest order, we expect that this will shift the Weyl nodes in a way that their momentum space configuration reflects the time-reversal symmetry breaking.

Keeping the above conceptual picture in mind, we now describe the calculated results of the Weyl node configuration of these two compounds. In CeAlGe, indeed, we found that the Weyl nodes are still the W1, W2, and W3 as in LaAlGe (Fig. 3**d**). The difference is that they are shifted away from the original location due to magnetism. In LaAlGe all W1 nodes can be related by symmetry operations. However, in CeAlGe, the inclusion of a magnetization along a direction gives rise to 4 inequivalent W1 Weyl nodes. They have different momentum space locations and energies. Similarly, there are now 4 inequivalent W2 and 8 inequivalent W3 Weyl nodes in CeAlGe because of the reduction of symmetries by the inclusion of the magnetization.

In PrAlGe, the magnetization along the c axis leads to 1 inequivalent W1, 2 inequivalent W2 and 2 inequivalent W3 Weyl nodes. More interestingly, we found the new Weyl nodes emerge, which we denote as the W4 nodes.

In order to understand how the Weyl nodes are shifted by the magnetization, we discuss the symmetry constraints in the presence of the ferromagnetic order in CeAlGe and PrAlGe (see Figs. 3**d**–**g**).

In CeAlGe, the magnetization is oriented along a axis. Both $\mathcal{T}$ and C_2 reverse this in-plane magnetization. However, their product $C_2\mathcal{T}$ is still a symmetry of the magnetic system and the same is true for M_x. Thus, all symmetry-nonequivalent Weyl nodes are found in the $k_x > 0$ part of the BZ depicted in Fig. 3**e**. Due to $C_2\mathcal{T}$, all W1- and W3-derived Weyl

nodes are still pinned to $k_z = 0$ and the W2-derived nodes are found in $\pm k_z$ pairs. It is also interesting to notice that the movement of the all Weyl nodes in the vicinity of the M_y ($//k_x$) mirror plane (W_1^1, W_1^2, W_2^2, and W_2^3), is much more significant than those of the M_x ($//k_y$) mirror plane (W_1^3, W_1^4, W_2^1, and W_2^4). This phenomenon is also symmetry related. Specifically, the Weyl nodes near the M_x ($//k_y$) mirror plane are roughly stationary upon magnetization because the symmetries $C_2\mathcal{T}$ and M_x are the only constraints to the effective Hamiltonian near the M_x mirror plane [11, 12]. However, this term turns out to be only relevant for the energy but not for the position of the Weyl nodes. The detailed information of the Weyl nodes including the momentum space locations, the energies and the type, is shown in the SI.

In PrAlGe, the magnetization is oriented along z. Both $\mathcal{T}$ and any of the mirror and glide mirror symmetries reverse this magnetization. However, their products, e.g., $\mathcal{T}M_x$, are still a symmetry of the magnetic system. Furthermore, C_{2z} and $\bar{C}_{4z}$ are preserved by the magnetization. Thus, all symmetry-nonequivalent Weyl nodes are found in a quadrant of the BZ depicted in Fig. 3**g**. The main difference to LaAlGe is that $C_{2z}\mathcal{T}$ symmetry is broken. As a result, we expect the W1 and W3 Weyl nodes to move along the k_z direction and become no longer pinned to $k_z = 0$. On the other hand, the W2 Weyl nodes are expected to stop appearing in $\pm k_z$ pairs.

We now describe the dispersion of the Weyl cones. In CeAlGe, we show the energy dispersion of the W_2^2 and W_2^4 Weyl cones in Figs. 4**d,e**. We see that the W2 are still type-II. Because the magnetization along the a direction breaks the mirror symmetry M_x, we see in Figs. 3**e** that the two W2 Weyl nodes in the vicinity of M_x, i.e., W_2^2 and W_2^3, are not symmetric with respect to this mirror any more. This can also be seen in the energy dispersions near W_2^2 in Fig. 4**d**. A schematic that summarizes the key properties of the Weyl fermions in CeAlGe is shown in Fig. 3**j**. Interestingly, we find that W1 also becomes type-II. The W1 and W3 Weyl nodes are far away from the Fermi level and therefore not relevant to low-energy physics. W2, which are type-II, are very close to the Fermi level. Therefore, CeAlGe is a $\mathcal{T}$-breaking type-II Weyl semimetal. The Weyl fermion dispersions of PrAlGe are shown in Figs. 4**f-h**. The dispersion in (E, k_x, k_y) space of the newly generated W4 Weyl cone is shown in Fig. 4**f**, from which we see that W4 are type-I. Figures 4**g,h** show the dispersion and Fermi surface of a W1 Weyl cone. We see that the W1 Weyl cones in PrAlGe also become type-II. We further observe that the W1 Weyl nodes are shifted away

from the $k_z = 0$ plane (Fig. 4**h**). In fact, the two adjacent W1 nodes move in opposite k_z directions. As a result, the Fermi surface at a constant k_z (Fig. 4**h**) only reveals one Weyl node. A schematic summary is shown in Fig. 3**k**. Interestingly, W2 is pushed to be well above the Fermi level. On the other hand, W3 and W4, which are of type-I, are now close to the Fermi level. Therefore, PrAlGe is a $\mathcal{T}$-breaking type-I Weyl semimetal.

A new route to realizing $\mathcal{T}$-breaking Weyl fermions

Our theoretical discovery of CeAlGe and PrAlGe reveals a new route to realizing $\mathcal{T}$-breaking Weyl fermions. The traditional and commonly accepted proposal for realizing $\mathcal{T}$-breaking Weyl fermions is to break time-reversal symmetry of a 3D Dirac fermion system, as shown in Figs. 5**a,b**. In this way, the Weyl fermions actually arise from the breaking of time-reversal symmetry. We can qualitatively understand the anomalous Hall effect. As shown in Fig. 5**b**, we consider the Chern number of a series of (k_y, k_z) 2D slices at different k_x-intercepts. Any slice between the left boundary of the BZ and the first dotted line has a Chern number of 0. As we continue sweeping the (k_y, k_z) slice to the right, we pass through the blue Weyl node and therefore the Chern number changes by 1. Consequently, a slice between the first dotted line and the second dotted line has a Chern number of 1. Then we pass the red Weyl node and the Chern number of a slice between the second dotted line and the right boundary of the BZ is 0. As a result, the Chern number averaged over all k_z in the BZ is nonzero, which demonstrates the existence of an anomalous Hall effect. It can be checked that this simple consideration carries over to CeAlGe and PrAlGe, despite the presence of additional symmetries, and an anomalous Hall effect is expected in the plane perpendicular to the respective magnetization. By contrast, in the Dirac semimetal case in Fig. 5**a**, the Chern number of any slice is zero, consistent with the fact that Dirac semimetals do not show anomalous Hall conductance. In terms of experimental realization, this proposal means that one needs to introduce magnetism to a Dirac semimetal system such as $TlBi(S_{1-x}Se_x)_2$, Cd_3As_2 and Na_3Bi. Since these materials are nonmagnetic, one will need to dope the system with magnetic dopants, which has been proven to be quite difficult. It is also challenging to systematically study the band structure of the magnetically doped system through first-principles calculations.

We now elaborate on our new route to realizing $\mathcal{T}$-breaking Weyl fermions as demonstrated in CeAlGe and PrAlGe. Rather than starting from a Dirac semimetal, we start

from a space-inversion ($\mathcal{I}$) breaking Weyl semimetal. As schematically shown in Fig. 5**c**, two pairs of Weyl nodes are generated by the breaking of space inversion symmetry. In this case, magnetization is only responsible for shifting the momentum space location of the Weyl nodes. We note that a $\mathcal{T}$-breaking Weyl semimetal is defined as the breaking of time-reversal symmetry in terms of the Weyl node configuration. Specifically, Weyl nodes of same chirality cannot appear at opposite momenta ($\pm\vec{k}$). Therefore, although in this case the Weyl fermions do not arise from ferromagnetism, the system in Fig. 5**d** still counts as a $\mathcal{T}$-breaking Weyl semimetal. This can also be seen by studying the Chern number of the (k_y, k_z) 2D slices. As shown in Figs. 5**c,d**, introducing magnetism leads to a finite k_x range at which the Chern number of the (k_y, k_z) 2D slice is nonzero. This also suggests the existence of anomalous Hall conductance in the system shown in Fig. 5**d**. We emphasize a number of advantages of this new route. Introducing magnetism is done by going from LaAlGe to CeAlGe or PrAlGe rather than doping. This not only avoids the complicated doping processes, but also enables to systematically understand the band structure in calculations as we have achieved here. Moreover, the displacement of the Weyl nodes upon including magnetism is easily understood at a qualitative level by considering a Zeeman coupling. To some extend, this is similar to the Zeeman effect caused by an external magnetic field, but obviously the intrinsic magnetism has a much stronger effect. Furthermore, our results demonstrate an entirely new way to search for $\mathcal{T}$-breaking Weyl semimetals in future, i.e., to look for the iso-chemical ferromagnetic cousin compounds of an $\mathcal{I}$-breaking Weyl semimetal.

Tunability of the RAlX Weyl family

Finally, we highlight the unparalleled tunablity of the RAlX family. As we have shown here, the low-energy band structures of LaAlGe, CeAlGe and PrAlGe realize the $\mathcal{I}$-breaking type-II, the $\mathcal{T}$-breaking type-II, and the $\mathcal{T}$-breaking type-I Weyl fermions. Moreover, n (electron) doping can be achieved by changing the ratio between Al and Ge, i.e., $RAl_{1-x}Ge_{1+x}$ [36], which will enable one to access other Weyl nodes that are above the Fermi level (Figs. 3**i-k**). We also briefly discuss the antiferromagnetic compounds SmAlGe and GdAlGe in this family. As we have explained in detail above, the lack of space-inversion symmetry of the RAlGe crystals already gives rise to Weyl fermions. Now, instead of the ferromagnetism, we need to consider the effect of antiferromagnetism (AFM) in SmAlGe and GdAlGe. Qualitatively, AFM will lead to BZ folding, which introduces new Weyl nodes into the system.

Additionally, the Kondo effect may play a role (especially for the Sm-based compounds) if the f-band is located close to the Fermi level, which can bring strong electronic interactions to the Weyl fermionic system. Currently, the detailed configuration of the AFM ordering in SmAlGe and GdAlGe has not been measured experimentally, which hinders us from systematically calculating their band structure. In general, RAlX is an extremely rich system that enables one to systematically study all types of Weyl fermions in a single family. This represents a significant breakthrough in identifying Weyl fermion materials.

METHODS

The first-principles calculations were performed within the density functional theory (DFT) framework using the projector augmented wave method [40] as implemented in the VASP [41] package and full-potential augmented plane-wave method as implemented in the package Wiek2k. The generalized gradient approximation (GGA) [42] was used for the exchange-correlation effect and the Hubbard energy U used in the calculation is 4 eV. The lattice constants of RAlX were acquired from previous experimental measurements [34–36]. A Γ-centered k-point $14 \times 14 \times 14$ mesh was used and spin-orbit coupling was included in the self-consistent cycles.

[1] Hasan, M. Z. & Kane, C. L. Colloquium: Topological insulators. *Rev. Mod. Phys.* **82**, 3045-3067 (2010).

[2] Qi, X.-L. & Zhang, S.-C. Topological insulators and superconductors. *Rev. Mod. Phys.* **83**, 1057-1110 (2011).

[3] Hasan, M. Z., Xu, S.-Y., & Neupane, M. Topological Insulators, Topological semimetals, Topological Crystalline Insulators, and Topological Kondo Insulators. in *in Topological Insulators: Fundamentals and Perspectives* edited by F. Ortmann, S. Roche, S. O. Valenzuela (John Wiley & Sons, 2015).

[4] Hasan, M. Z., Xu, S.-Y., & Bian, G. Topological Insulators, Helical Topological Superconductors and Weyl Fermion Semimetals. *Phys. Scr.* **T164**, 014001 (2015).

[5] Weyl, H. Elektron und gravitation. *Z. Phys.* **56**, 330-352 (1929).

[6] Herring, C. Accidental Degeneracy in the Energy Bands of Crystals. *Phys. Rev.* **52**, 365-373 (1937).

[7] Volovik, G. E. *The Universe in a Helium Droplet* (Oxford University Press, 2003).

[8] Murakami, S. Phase transition between the quantum spin Hall and insulator phases in 3D: emergence of a topological gapless phase. *New J. Phys.* **9**, 356 (2007).

[9] Wan, X., Turner, A. M., Vishwanath, A. & Savrasov, S. Y. Topological semimetal and Fermi-arc surface states in the electronic structure of pyrochlore iridates. *Phys. Rev. B* **83**, 205101 (2011).

[10] Burkov, A. A. & Balents, L. Weyl Semimetal in a Topological Insulator Multilayer. *Phys. Rev. Lett.* **107**, 127205 (2011).

[11] Huang, S. M. *et al.* A Weyl Fermion semimetal with surface Fermi arcs in the transition metal monopnictide TaAs class. *Nature Commun.* **6**, 7373 (2015).

[12] Weng, H., Fang, C. Fang, Z. Bernevig, A. & Dai, X. Weyl semimetal phase in non-centrosymmetric transition metal monophosphides. *Phys. Rev. X* **5**, 011029 (2015).

[13] Xu, S.-Y. *et al.* Discovery of a Weyl fermion semimetal and topological Fermi arcs. *Science* **349**, 613-617 (2015).

[14] Lu, L. *et al.* Observation of Weyl points in a photonic crystal. *Science* **349**, 622 (2015).

[15] Lv, B. Q. *et al.* Experimental Discovery of Weyl Semimetal TaAs. *Phys. Rev. X* **5**, 031013 (2015).

[16] Soluyanov, A. A. *et al.* Type II Weyl Semimetals. *Nature* **527**, 495-498 (2015).

[17] Nielsen, H. B. & Ninomiya, M. The Adler-Bell-Jackiw anomaly and Weyl fermions in a crystal, *Physics Letters B*, **130**, 389-396 (1983).

[18] Parameswaran, S. A. *et al.* A. Probing the chiral anomaly with nonlocal transport in three-dimensional topological semimetals. *Phys. Rev. X* **4**, 031035 (2014).

[19] Potter, A. C., Kimchi, I. & Vishwanath, A. Quantum oscillations from surface Fermi-arcs in Weyl and Dirac semi-metals. *Nature Commun.* **5**, 5161 (2014).

[20] Baum, Y., Berg, E., Parameswaran, S. A. & Stern, A. Current at a Distance and Resonant Transparency in Weyl Semimetals. *Phys. Rev. X* **5**, 041046 (2015).

[21] Zyuzin, A. A. & Burkov, A. A. Topological response in Weyl semimetals and the chiral anomaly. *Phys. Rev. B* **86**, 115133 (2012)

[22] A. A. Burkov, Anomalous Hall Effect in Weyl Metals, *Phys. Rev. Lett.* **113**, 187202 (2014)

[23] Kargarian, M., Randeria, M. & Trivedi, N. *Sci. Rep.* **5**, 12683 (2015)

[24] Xu, G. *et al.* Chern semi-metal and quantized anomalous Hall effect in $HgCr_2Se_4$. *Phys. Rev. Lett.* **107,** 186806 (2011).

[25] Owerre, S. A. Weyl semimetal in ultra-thin film of topological insulator multilayer. Preprint at http://arxiv.org/abs/1601.03707 (2016)

[26] Hosur, P. & Qi, X.-L. Time-reversal invariant topological superconductivity in doped Weyl semimetals.*Phys. Rev. B.* **90**, 045130 (2014).

[27] Li, Y. & Haldane, F. D. M. Topological nodal Cooper pairing in doped Weyl seimetals. Preprint

at http://arxiv.org/abs/1510.01730 (2015).

[28] Kim, Y., Park, M. J. & Gilbert, M. J. Probing unconventional superconductivity in inversion symmetric doped Weyl semimetal. http://arxiv.org/abs/1604.01040 (2016).

[29] Sun, Y. *et al.* Prediction of the Weyl semimetal in the orthorhombic $MoTe_2$. *Phys. Rev. B* **92**, 161107 (2015).

[30] Chang, T.-R. *et al.* Prediction of an arc-tunable Weyl Fermion metallic state in $Mo_xW_{1-x}Te_2$. *Nature Commun.* **7**,10639 (2016).

[31] Wang, Z. *et al.* Time-Reversal Breaking Weyl Fermions In Magnetic Heuslers. Preprint at http://arxiv.org/abs/1603.00479 (2016).

[32] Chang, G. *et al.* Room-temperature magnetic topological semimetal state in half-metallic Heusler Co_2TiX (X=Si, Ge, or Sn). Preprint at http://arxiv.org/abs/1603.01255 (2016).

[33] Xu, S.-Y. *et al.* Discovery of Lorentz-violating Weyl fermion semimetal state in LaAlGe materials. Preprint at http://arxiv.org/abs/1603.07318 (2016).

[34] Guloy, A. M. & Corbett, J. D. Syntheses and structures of LaAlGe: Interrelationships among the alpha-$ThSi_2$, alpha-$GdSi_2$, and LaPtSi structure type. *Inorg. Chem.* **30**, 4789-4794 (1991).

[35] Dhar, S. K. & Corbett, S. M. Structural and magnetic properties of $CeAl_xSi_{2-x}$ and $CeAl_xGe_{2-x}$. *Journal of Magnetism and Magnetic Materials* **152**, 22-26 (1996).

[36] Gladyshevskii, E. I., Nakonechna, N. Z., Cenzual, K., Gladyshevskii, R. E. & Jorda, J. L. Crystal structures of $PrAl_xGe_{2-x}$ compounds. *Journal of Alloys and Compounds* **296**, 265-271 (2000).

[37] Bobev S., Tobash P.H., Fritsch V., Thompson J. D., Hundley M. F., Sarrao J. L. & Fisk Z. Ternary rare-earth alumo-silicides-single-crystal growth from Al flux, structural and physical properties. *Journal of Solid State Chemistry* **178**, 2091-2103 (2005).

[38] Lu, H., Zhang, X., Bian, Y. & Jia, S. In preparation.

[39] Flandorfer, H., Kaczorowski, D., Gröbner, J., Rogla, P., Wouters, R., Godart, C. & Kostikasg, A. The Systems Ce-Al-(Si, Ge): Phase Equilibria and Physical Properties. *Journal of Solid State Chemistry* **137**, 191-205 (1998).

[40] Kresse, G., & Joubert, D., From ultrasoft pseudopotentials to the projector augmented-wave method. *Physical Review B* **59**, 1758-1775 (1999).

[41] Kresse, G. & Furthmller, J., Efficiency of *ab*-initio total energy calculations for metals and semiconductors using a plane-wave basis set. *Computational Materials Science* **6**, 15-50 (1996).

[42] Perdew, J. P., Burke, K. & Ernzerhof, M. Generalized Gradient Approximation Made Simple. *Phys. Rev. Lett.* **77**, 3865-3868 (1996).

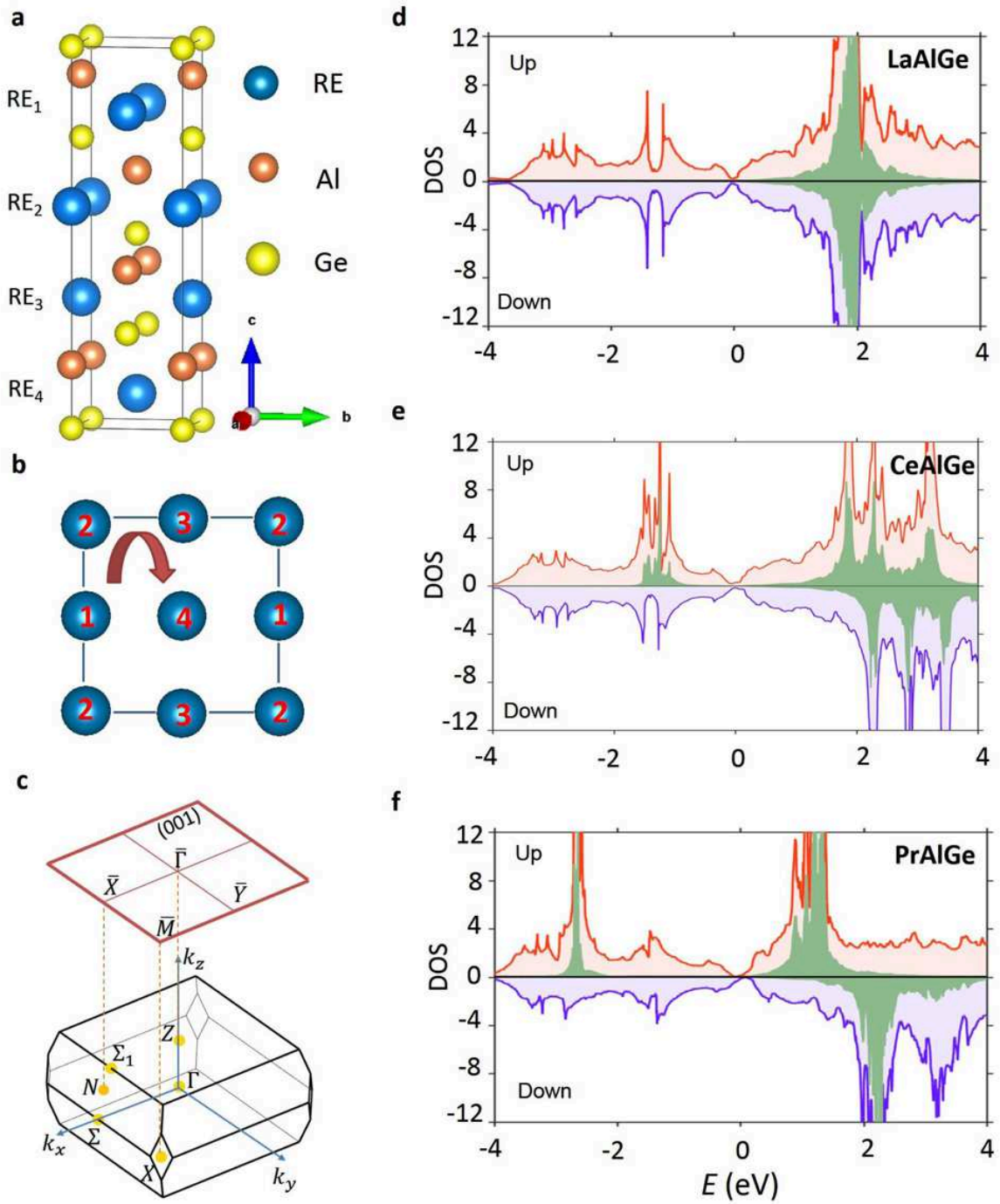

FIG. 1: **Lattice structure, Brillouin zone and density of state (DOS) of RAlGe (R=La, Ce, and Pr).** (**a**) Body-centered tetragonal structure of RAlGe, with space group $I4_1md$ (109). The structure consists of stacks of rare earth element (RE), Al, and Ge layers and along the (001) direction each layer consists of only one type of elements. (**b**) The schematic of RE atomic layer showing the skew axis along the c axis. (**c**) The bulk and (001) surface Brillouin zone (BZ). (**d-f**) First-principles DOS of LaAlGe (**d**), CeAlGe (**e**) and PrAlGe (**f**). The partial DOS for spin-up and spin-down states are plotted in red and violet colors, respectively. The DOS from localized f orbitals are drawn in green color.

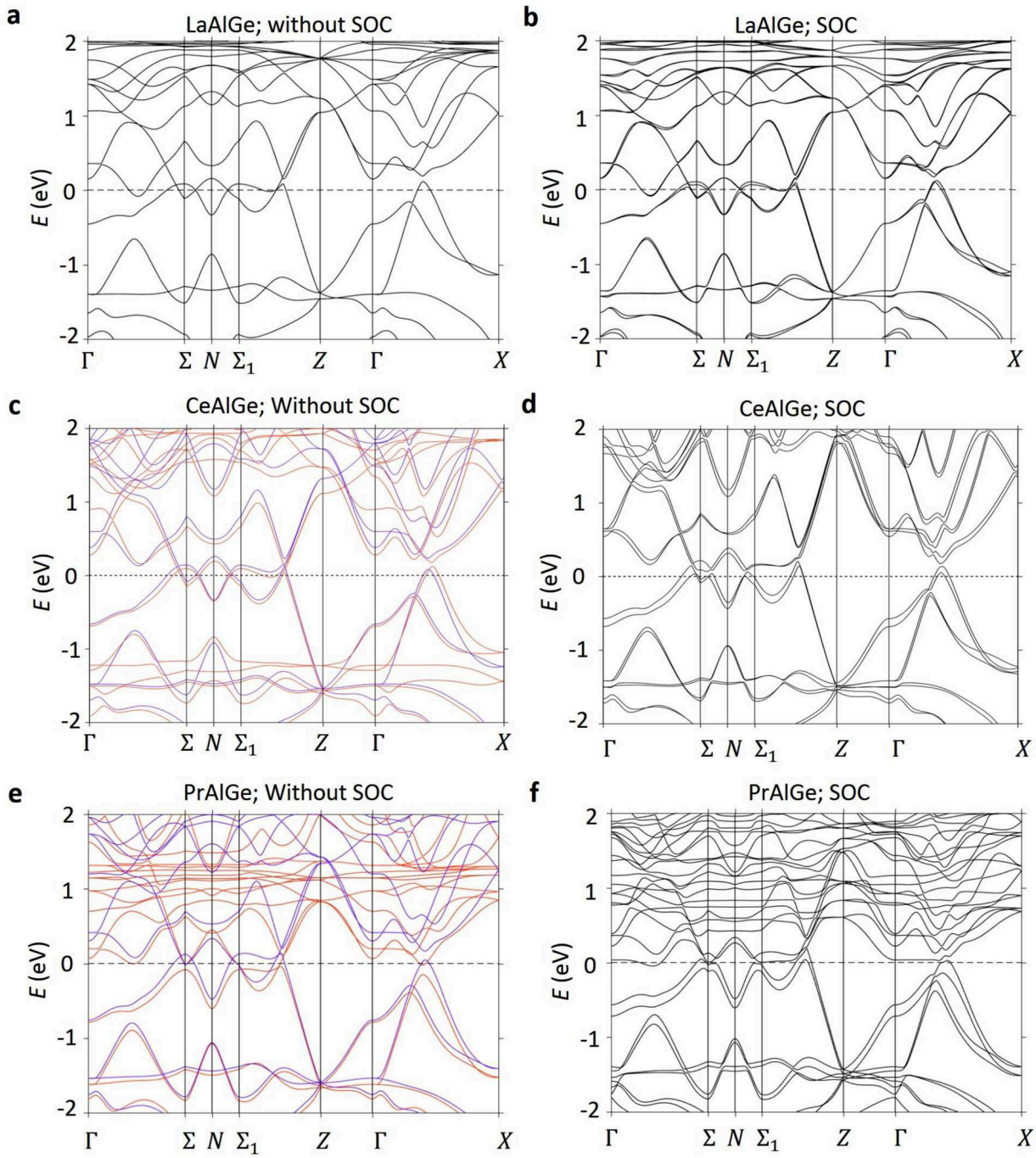

FIG. 2: **First-principles band structure of RAlGe (R=La, Ce, and Pr).** (**a,b**) Calculated bulk band structure of LaAlGe without and with the inclusion of spin-orbit coupling. (**c,d**) Bulk band structure of CeAlGe without and with the inclusion of spin-orbit coupling. In **c** the bands of spin-up and spin-down states are plotted in red and violet colors, respectively. (**e,f**) same as (**c,d**) but for PrAlGe.

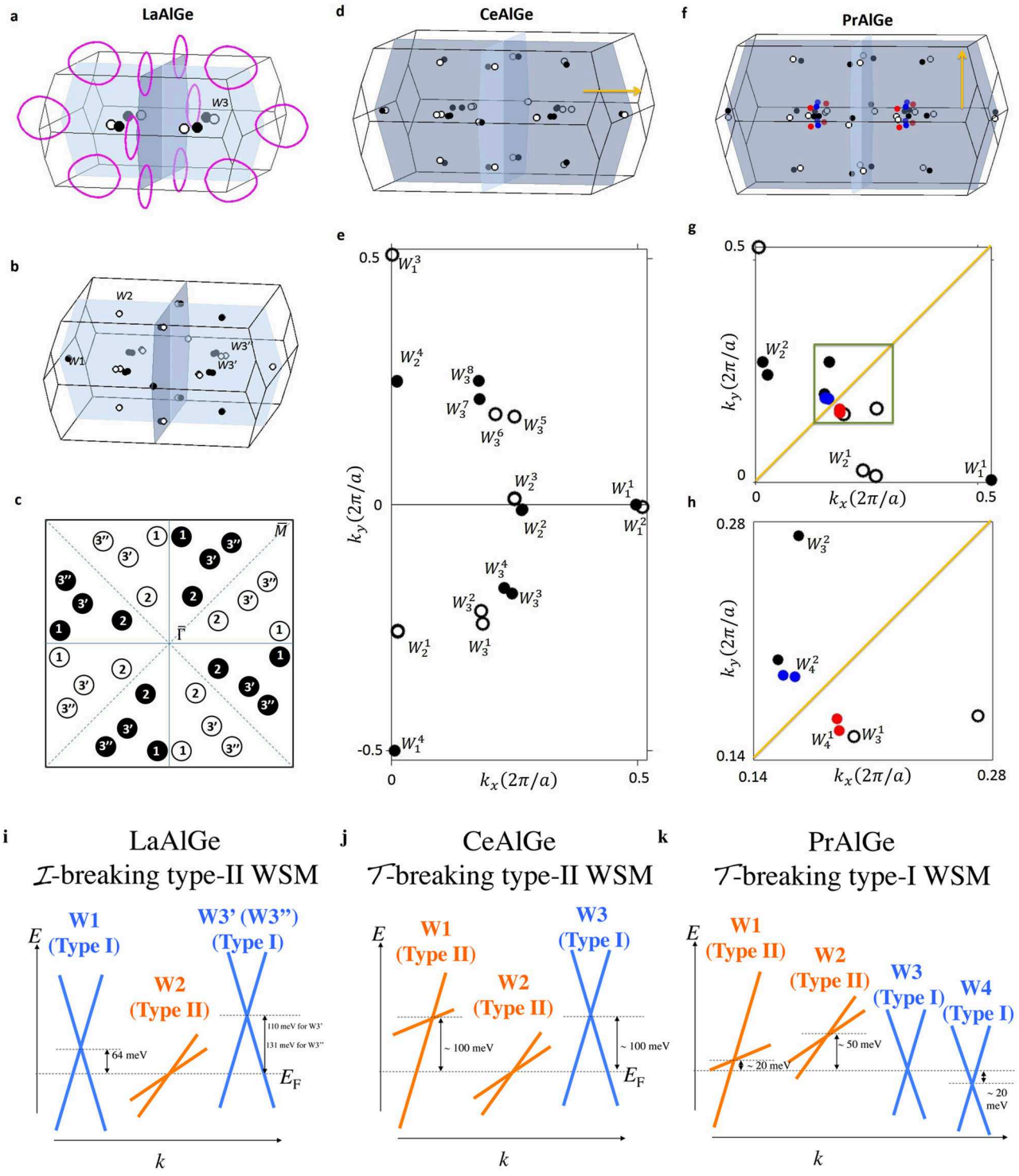

FIG. 3: **Weyl fermions in LaAlGe, CeAlGe, and PrAlGe.**

FIG. 3: (**a**) The nodal lines and Weyl nodes (denoted by W3) in the first BZ of LaAlGe without the inclusion of SOC. (**b**) Configuration of Weyl nodes in the first BZ of LaAlGe with the inclusion of SOC. (**c**) Projection of the Weyl nodes on the (001) surface Brillouin zone (SBZ) of LaAlGe. (**d**) Same as **b** but for CeAlGe. The arrow indicates the magnetization orientation of localized f orbitals of Ce. (**e**) Projection of the Weyl nodes on a half of the (001) SBZ of CeAlGe. The configuration of the other half of the SBZ can be obtained by considering mirror symmetry. (**f**) Same as **b** but for PrAlGe. The red and blue dots denote the emergent Weyl nodes generated by the magnetization of f orbitals of Pr. The arrow indicates the magnetization orientation. (**g**) Projection of the Weyl nodes of PrAlGe in one quadrant of the (001) SBZ. (**h**) Zoomed-in configuration of Weyl nodes shown in the green box in **g**. (**i-k**) Schematic of the band dispersion of Weyl fermions in LaAlGe, CeAlGe, and PrAlGe, respectively.

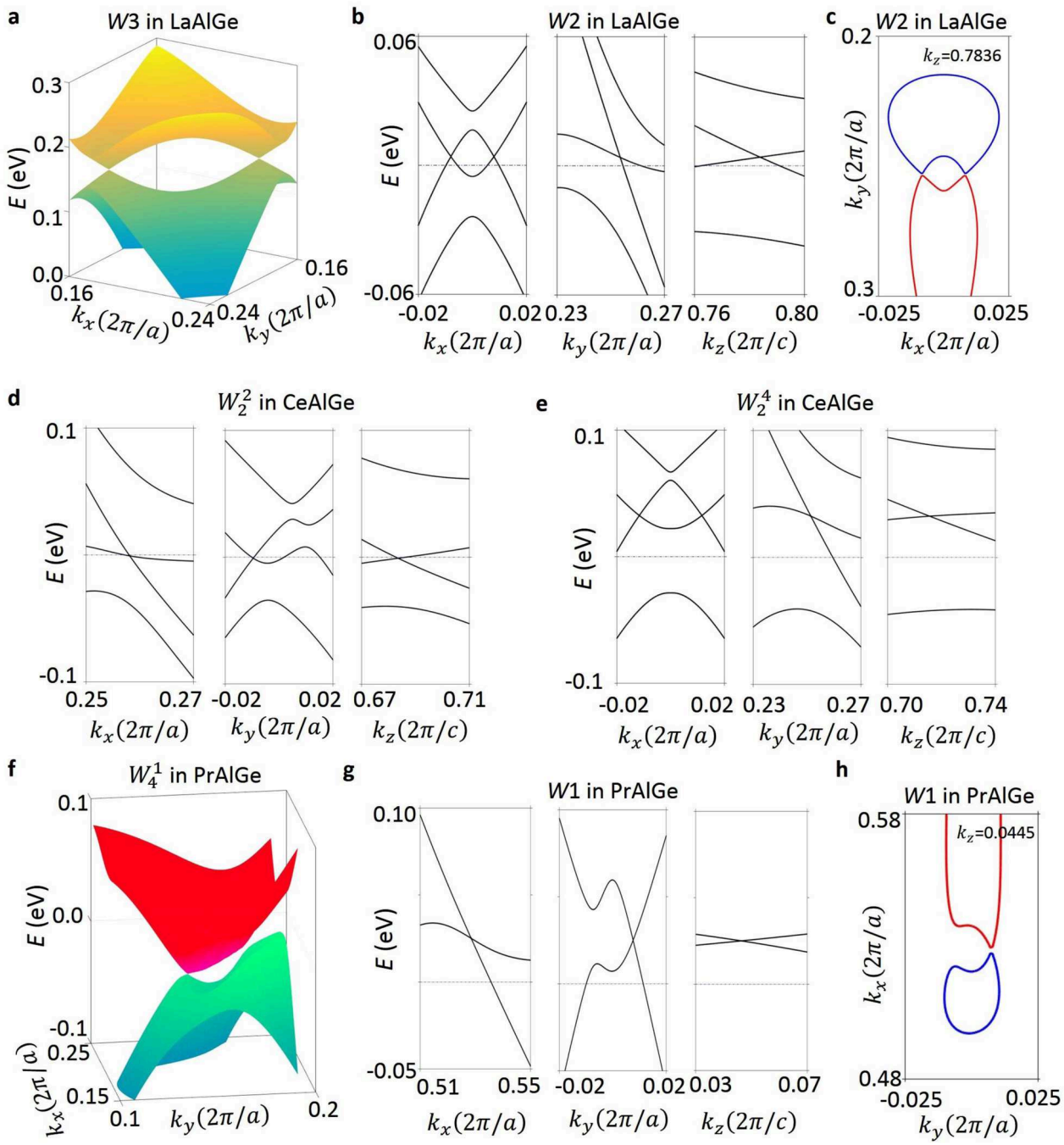

FIG. 4: **Band dispersion of Weyl quasi-particles in LaAlGe, CeAlGe, and PrAlGe.** (**a**) The bulk band structure close to $W3$ Weyl nodes in LaAlGe. (**b**) The linear band dispersion along three momentum directions showing the type-II Weyl fermion nature of the $W2$ node in LaAlGe. (**c**) calculated constant energy band contour in the k_z=0 plane at the energy of the W2 nodes of LaAlGe. Blue lines correspond to hole-like pockets, whereas red lines indicate electron-like pockets. (**d**) Same as **b**, but for W_2^2 Weyl nodes in CeAlGe. (**e**) Same as **b**, but for W_2^4 Weyl nodes in CeAlGe. (**f**) Same as **a** but for W_4^1 Weyl nodes in PrAlGe. (**g**) Same as **b**, but for $W1$ Weyl nodes in PrAlGe. (**h**) Same as **c**, but for $W1$ Weyl nodes in PrAlGe in the k_z=0.0445 plane.

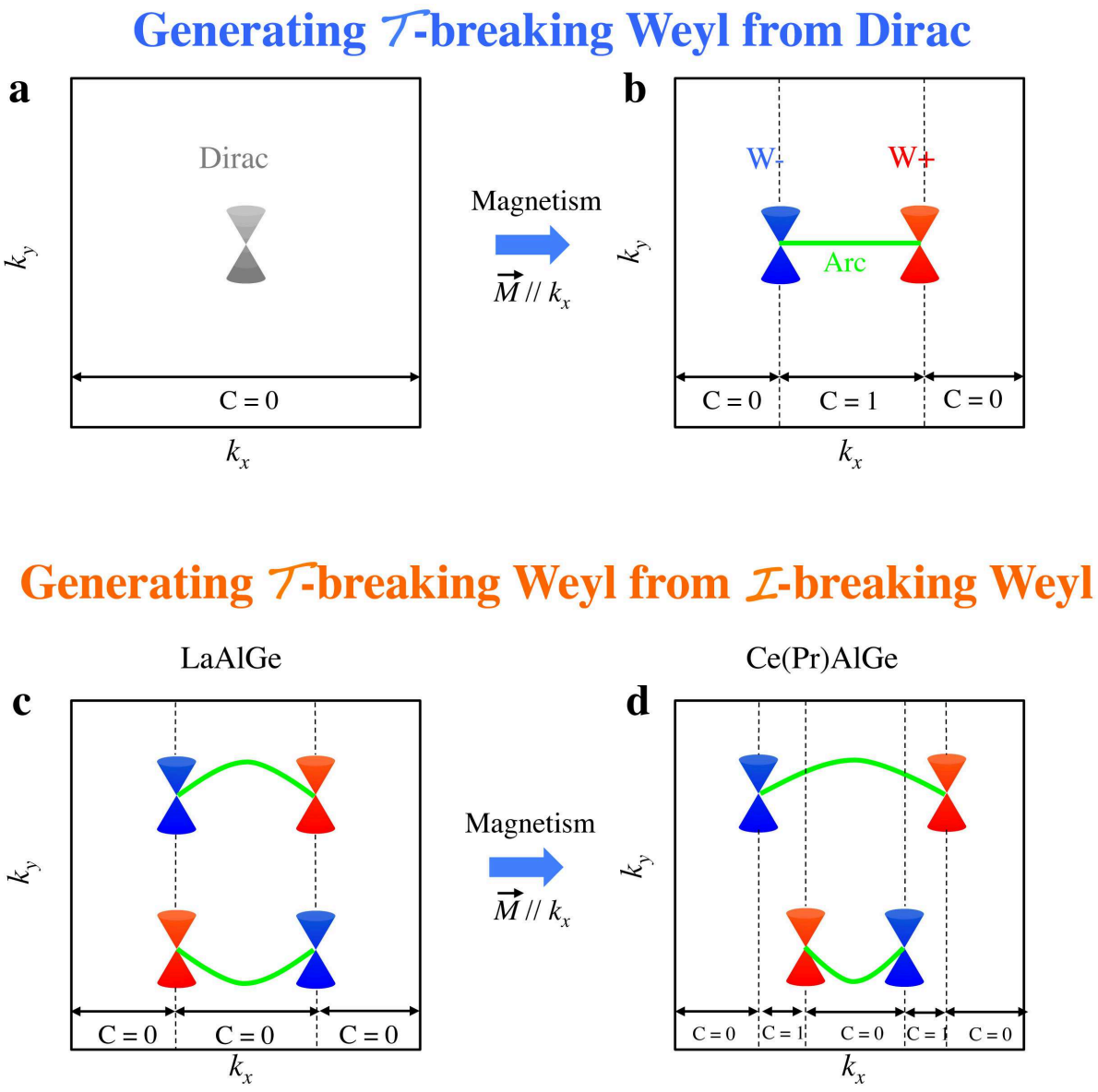

FIG. 5: **A new route to generating magnetic Weyl fermions.** (**a,b,**) The Dirac node in a Dirac semimetal splits into a pair of Weyl nodes upon the inclusion of a magnetic field. The Weyl nodes are connected by a Fermi arc surface state. (**c,d,**) Two pairs of Weyl nodes are present in a inversion-breaking Weyl semimetal. The Weyl nodes are shifted in momentum space upon the inclusion of a magnetic field, generating regions in $\boldsymbol{k}$ space with a non-zero Chern number.